12-4-2019

A Numerical Investigation on the Variation of Sodium Ion and Observed Thermospheric Sodium Layer at Cerro Pachón, Chile During Equinox

Xuguang Cai
Utah State University, Center for Atmospheric and Space Science

Tao Yuan
Utah State University, Center for Atmospheric and Space Science

J. Vincent Eccles
Space Environment Corporation

N. M. Pedatella
National Center for Atmospheric Research

Xiaoqi Xi
Utah State University, Center for Atmospheric and Space Science

See next page for additional authors

Scholarly Commons Citation

Cai, X., Yuan, T., Eccles, J. V., Pedatella,N. M., Xi, X., Ban, C., & Liu, A. Z.(2019). A Numerical Investigation onthe Variation of Sodium Ion andObserved Thermospheric Sodium Layerat Cerro Pachón, Chile DuringEquinox. Journal of GeophysicalResearch: Space Physics, 124,https://doi.org/10.1029/2018JA025927

JGR Space Physics

RESEARCH ARTICLE
10.1029/2018JA025927

Key Points:
- Fountain effect does not have much influences on the structure of Na over subtropics region of geomagnetic equator during night
- The thermospheric Na layer observed over Cerro Pachón, Chile is probably formed due to the large vertical wind perturbation
- The large vertical wind perturbation that may generate thermospheric Na layer is closely associated with semidiurnal tide

Correspondence to:
X. Cai,
cxg1106@msn.cn

Citation:
Cai, X., Yuan, T., Eccles, J. V., Pedatella, N. M., Xi, X., Ban, C., & Liu, A. Z. (2019). A Numerical Investigation on the Variation of Sodium Ion and Observed Thermospheric Sodium Layer at Cerro Pachón, Chile During Equinox. *Journal of Geophysical Research: Space Physics*, *124*, 10,395–10,414 https://doi.org/10.1029/2018JA025927

Received 20 JUL 2018
Accepted 3 SEP 2019
Accepted article online 14 OCT 2019
Published online 04 DEC 2019

A Numerical Investigation on the Variation of Sodium Ion and Observed Thermospheric Sodium Layer at Cerro Pachón, Chile During Equinox

Xuguang Cai[1,2], Tao Yuan[1,2], J. Vincent Eccles[3], N. M. Pedatella[4], Xiaoqi Xi[1,2], Chao Ban[5], and Alan Z. Liu[6]

[1]Department of Physics, Utah State University, Logan, UT, USA, [2]Center for Atmospheric and Space Science, Logan, UT, USA, [3]Space Environment Corporation, Providence, UT, USA, [4]High Altitude Observatory, National Center for Atmospheric Research, Boulder, CO, USA, [5]Institute of Atmospheric Physics, Chinese Academy of Sciences, Beijing, China, [6]Center for Space and Atmospheric Research and Department of Physical Sciences, Embry-Riddle Aeronautical University, Daytona Beach, FL, USA

Abstract The extension of the neutral sodium (Na) layer into the thermosphere (up to 170 km) has recently been observed at low and high latitudes using a Na lidar. However, the geophysical mechanisms and implications of its formation are currently unknown. In this study, we conduct an advanced two-dimensional numerical simulation of the Na and Na^+ variations in the *E* and *F* regions at low latitudes. The numerical simulations are used to investigate the contributions of the electromagnetic force, neutral wind, diffusion, and gravity. The simulations lead to three major findings. First, Na^+ in the subtropical region of the geomagnetic equator acts as the major reservoir of the neutral sodium, and its distribution during nighttime is mostly below 200 km due to the combined effect of the vertical component of the $\vec{E}\times\vec{B}$ drift and Coulomb-induced drift. Second, we find that the fountain effect has little influence on the behavior of Na in the nighttime. Third, the probable explanation for the frequent generation of the thermospheric sodium layer during spring equinox at Cerro Pachón, Chile is attributed to the large vertical neutral transport generated by large vertical wind perturbations of unknown origin, with a magnitude exceeding 10 m/s that is closely associated with the semidiurnal tide.

1. Introduction

The sodium metal layer, usually formed between about 75 and 110 km in the mesosphere and lower thermosphere (MLT), has been investigated for several decades by the observations from resonance lidars and satellites (Clemesha, Batista, et al., 2004; Fussen et al., 2010; Gardner et al., 2005; Gumbel et al., 2007; She et al., 2000; States & Gardner, 1999; Yi et al., 2009; Yuan et al., 2012). Sporadic sodium layers also exist and are characterized by the sharp Na density enhancement forming in the mesopause region (80–105 km) with the layer thickness of a few kilometers (Clemesha, 1995). Most sporadic Na layers are observed below 120 km (Yi et al., 2007; Yuan et al., 2014). However, recent studies (see references presented in the following) have also revealed the existence of an extended sodium (along with other metal atoms) layer that extends into the thermosphere, reaching altitudes well above 120 km, where the molecular diffusion is larger than eddy diffusion. Unlike the sporadic metal layers described before, these thermospheric extensions can be as high as 10 to 50 km above the main layer and last for several hours. Thermospheric metal layers have been observed at McMurdo, Antarctica (69°S, 78°E; Chu et al., 2011) in May 2011; Davis, Antarctica (69°S, 78°E; Lübken et al., 2011) in January 2011; Beijing, China (40.2°N, 116°E) in May 2010 (Wang et al., 2012); Lijiang, China (26.7°N, 100°E) in March and April 2012 (Xue et al., 2013); Arecibo, Puerto Rico (18.35°N, 66.8°W) in March 2005 (Friedman et al., 2013); and Syowa, Antarctica (69°S, 39.6°E) in September 2000 (Tsuda et al., 2015). Gao et al. (2015) reported on 12 thermospheric Na layers at Lijiang, China that occurred in March, April, and December 2012, with at least four of them extending up to 170 km and gave a qualitative explanation on the formation of these thermospheric Na layers. They argued that the layers are formed due to tidal modulation and the recombination reaction between electrons and Na^+ transported by the fountain effect. It is the phenomenon that the $\vec{E}\times\vec{B}$ drift uplifts ions near geomagnetic equator to higher altitudes in the daytime, and then gravity and diffusion redistribute ions along the magnetic field lines (mainly in meridional direction) downward and away from geomagnetic equator

during nighttime. Liu et al. (2016) first reported on the occurrence of a thermospheric Na layer up to 150 km at the Andes Lidar Observatory (ALO) in Cerro Pachón, Chile (30.25°S and 70.74°W geographic, and 20°S in magnetic latitude). The Na lidar in Cerro Pachón, Chile has subsequently observed as many as 23 thermospheric Na layer events during the second half of the night during equinox. These previous studies illustrate that most of the thermospheric metal layers are observed at high latitudes and low geomagnetic/geographic latitudes, and there are fewer reports of thermospheric metal layers occurring at midlatitudes.

Since Na^+ in the *E* and lower *F* region is the main reservoir for neutral sodium, and their correlations are well documented (Daire et al., 2002; Delgado et al., 2012; Dou et al., 2010; Friedman et al., 2000; Heinrich et al., 2008; Yuan et al., 2013; Yuan, Wang, et al., 2014), it is essential to understand the variation of metal ions in the thermosphere. Carter and Forbes (1999) developed a two-dimensional (2-D) model to investigate the behavior of Fe^+ between 0° and 45°N at 67°W and they found that descending Fe^+ layers could be produced over Arecibo, Puerto Rico due to the tidal winds. Chu and Yu (2017) used a numerical simulation to investigate the thermospheric Fe layer over McMurdo, Antarctica and argued that the thermospheric Fe layer was attributed to the combined effects of direct recombination of Fe^+ and electrons, as well as large (relative to the mean) amplitude vertical wind modulation caused by gravity waves, aurora, and horizontal wind divergence. Using a 1-D numerical model, Cai et al. (2017) investigated the variations of the summertime Na in the midlatitude *E* region above North America due to tidal waves and gravity waves. The investigation concluded that large vertical transport generated by tidal vertical wind modulations could be the deciding factor in these Na layer events (sporadic Na layer) in the lower *E* region (<120 km) where the electromagnetic forces are weak. Although thermospheric sodium layers (TSLs) have been observed at low geomagnetic/geographic latitudes, such as ALO at Cerro Pachón, Chile and Lijiang, China, there has not been a detailed study of their formation mechanisms. Different mechanisms may be responsible for TSLs at these locations since both neutral and electromagnetic effects influence ions at low geomagnetic/geographic latitudes.

To investigate the behaviors of Na and Na^+ at ALO in Cerro Pachón, Chile (30.25°S, 70.74°W), we have built an extended 2-D numerical model (full vertical and meridional transport with simplified zonal transport) that covers both sides of the geomagnetic equator and include both chemical and dynamical effects. This model extends our previous numerical framework (Cai et al., 2017), utilizing the Na neutral and ion-molecular chemical reactions of Plane et al. (2015), together with transport effects caused by neutral winds, electromagnetic field, gravity, and diffusion. The model is applied to study the density variations of Na and Na^+ during April in the equatorial *E* and *F* region. The paper is outlined as follows. Section 2 presents the detailed information of the numerical model and a brief description of four separate simulations to study Na and Na^+ variations driven by two large-scale models, together with the influence of fountain effect and contributions of vertical and horizontal transport on Na and Na^+. In section 3, we first present the observation of TSLs at ALO, and then conduct four numerical simulations, resulting in a proposed potential mechanism for TSLs. The conclusion and broader context of the results are presented in section 4.

2. Modeling Na/Na^+ Variations Near the Geomagnetic Equator

2.1. Numerical Framework

Based on the 1-D model discussed in Cai et al. (2017), we have developed an extended 2-D model that solves the continuity equations of the neutrals and ions relevant to Na chemistry in meridional (*y*) and vertical (*z*) directions:

$$\frac{\partial N_M}{\partial t} = S_M + P_M - L_M - \nabla \bullet \left(N_M \vec{V}_M \right), \tag{1}$$

where N_M represents the number density of species *M* (when we refer to "density of XX (species)" later, we always mean number density) and *t* is the universal time (UT). $\underline{S_M}$ is the source function, which is the input rate of the number density of species *M*. P_M and L_M are the chemical production and loss rates of the number density of species *M*, respectively. The last term on the right-hand side of equation (1) is the gradient of

Table 1
The Number of TSLs and Tidal-Featured TSLs Over ALO From May 2014 to January 2018

Month	Number of observation night	TSL
January	26	0
February	7	0
March	14	2
April	22	10
May	5	2
June	6	0
July	11	0
August	9	2
September	7	3
October	10	4
November	24	0
December	12	0

number density flux, where $\overrightarrow{V}_M$ represents the transport velocity of ions ($M = i$) or neutrals ($M = n$). The vertical range of the model is from 90 to 490 km with a vertical resolution of 2 km, and the meridional geographic range is from 44.5°S, 71°W to 18°N, 71°W, fully covering the geomagnetic equatorial region. There are 34 grid points in the latitudinal direction, which corresponds to a resolution of 1.9° (1°–111 km). The model computes the vertical and meridional transport precisely by the accurate flux-corrected transport (FCT) algorithm (Zalesak, 1979), which was designed for mass transportation to handle steep gradients of mass densities, as well as shock formation (Boris & Book, 1973). It combines a high-order solution to cancel out the diffusive errors and a low-order solution to limit the antidiffusive fluxes to maintain positivity through the use of flux limiter. The zonal transport term is $\left(\frac{\partial(N_M V_{Mx})}{\partial x} = N_M \frac{\partial V_{Mx}}{\partial x} + V_{Mx} \frac{\partial N_M}{\partial x}\right)$, where V_{Mx} is the zonal component of transport velocity and can be simplified to $N_M \frac{\partial V_{Mx}}{\partial x}$ because the horizontal gradients of the number density of a species are much smaller than the vertical gradient (Chu & Yu, 2017). It should be noted that our model's grid is still 2-D (y-z plane) and we only consider the nondiffusion terms in the zonal transport velocity, which can be directly calculated at each grid point. Note that the fountain effect, which is related to the vertical and meridional transport, plays an important role in the distribution of ions in the equatorial thermosphere and ionosphere. Therefore, we consider all terms in the vertical and meridional transport in our numerical simulations. Note that we refer to our model as an extended 2-D model because it incorporates a simplified zonal transport term, in addition to the full vertical and meridional transport. The parameters (temperature, wind, and electric field perpendicular to $\overrightarrow{B}$) used to drive the model have a 5-min resolution, and are incorporated to the model at each numerical time step (0.05 s) with linear interpolation. In this paper, we only consider geomagnetic quiet conditions.

The details of the source function and chemistry are similar to those presented in Cai et al. (2017, 2019), except that we have added the direct recombination reaction between Na^+ and electrons.

$Na^+ + e \rightarrow NA + h\nu$,, R1.

with the reaction rate coefficient of $3.0 \times 10^{-12}(T_n/200\ K)^{-0.74} cm^{-3} s^{-1}$, where T_n is the neutral temperature (Badnell, 2006). Cai et al. (2017) focused on altitudes below 120 km where the production or loss rate of R1 is much slower than many other Na/Na^+ reactions, and thus R1 could be ignored. However, Chu et al. (2011) and Chu and Yu. (2017) argued that the recombination reaction between metal ions and electrons might play important roles in the formation of thermospheric metal layers (extending up to 170 km). Therefore, we have included R1 into our current model. Below 120 km, the Na ion and neutral chemical reactions of Plane et al. (2015) are included. Above 120 km, only photoionization and the other major ionization processes of Na (R20, R21, and R35 in Table 1 in Plane et al. (2015)), together with R1 are included. For other reactions related to Na and Na^+, their production/loss rates are much smaller above 120 km due to decreased air density. In addition, some reactions are neglected because the temperature-dependent rate coefficients are valid only in a certain temperature range (Cox & Plane, 1998), while the temperature above 120 km increases rapidly.

2.1.1. Transport of Ions

As seen in equation (1), the variations of Na and Na^+ will not only be influenced by chemistry, but also by dynamical transport. In this section, we describe the transport of both ions and neutrals in detail. To describe the transport of Na^+, we utilize the simplified ion momentum equation (Schunk & Nagy, 2009),

$$\vec{\nabla} p_i - N_i m_i \vec{g} - eN_i\left(\vec{E} + \vec{V}_i \times \vec{B}\right) = N_i m_i \nu_m \left(\vec{u} - \vec{V}_i\right), \tag{2}$$

where $p_i = N_i k T_i$ is the ion pressure, N_i is the ion number density, and T_i is the ion temperature. m_i is the ion mass, e is the elementary charge, and $\vec{g}$ is the gravitational acceleration that changes with altitude and latitude. $\vec{V}_i$ is the ion transport velocity and $\vec{u} = (U, V, W)$ is the neutral wind, where U, V, and W are the zonal, meridional, and vertical wind components (hereafter simplified as the zonal/meridional/vertical wind). $\vec{E} = \left(E_x, E_y, E_z\right)$ is the electric field and $\vec{B} = (0, \cos I, \sin I)B_0$ is the Earth's magnetic field, where B_0 is the amplitude and I is the inclination angle (positive south of the geomagnetic equator). ν_{in} is the ion-neutral collision frequency, which is calculated based on Banks and Kockarts (1973) (see details in Cai et al., 2017). Note that $\vec{E}$ and $\vec{B}$ are both in Cartesian coordinates. The magnetic field values are from the International Geomagnetic Reference Field (IGRF). The electric fields are calculated for components perpendicular to $\vec{B}$ and parallel to $\vec{B}$ and then transformed into Cartesian coordinates. The electric fields perpendicular to $\vec{B}$ are obtained by combining the simple ionosphere electric field model results of Eccles (1998) and the field-line relationships from the appendix of Haerendel et al. (1992). These fields contribute to the $\vec{E}\times\vec{B}$ drift and Coulomb-induced drift. The electric field parallel to $\vec{B}$ is the polarization electrostatic field generated by the ambipolar diffusion characteristics of electrons and ions along the magnetic field line (Kelley, 2009). By solving equation (2) in Cartesian coordinates, we obtain the ion transport velocity ($\vec{V}_i$) components in the z and y directions:

$$V_u = V_{idz} + V_{izE\perp B} + V_{ezE//B} + V_{izu} + V_{izg} \tag{3}$$

$$V_{iy} = V_{idy} + V_{iyE\perp B} + V_{iyE//B} + V_{iyu} + V_{iyg} \tag{4}$$

Note that the ion transport velocity in the x direction is not shown here since we focus on the transport in the y and z directions. Both ion transport velocity components include two groups: one group is the ion velocity (vertical and meridional) containing the sum of the velocity due to the electric field perpendicular to $\vec{B}$ ($\vec{V}_{iE\perp B}$), gravity ($\vec{V}_{ig}$), and neutral wind ($\vec{V}_{iu}$). The other group can be attributed to ion-electron diffusion with the sum of ion diffusion ($\vec{V}_{id}$) and ambipolar diffusion ($\vec{V}_{iE//B}$).

For the ion diffusion terms:

$$V_{idz} = -\frac{r^2 + \sin^2 I}{1 + r^2}\left(\frac{D_i}{N_i}\frac{dN_i}{dz} + \frac{k}{m_i \nu_{in}}\frac{dT}{dz}\right) - \frac{\cos I \sin I}{1 + r^2}\left(\frac{D_i}{N_i}\frac{dN_i}{dy}\right), \tag{5}$$

$$V_{idy} = -\frac{r^2 + \cos^2 I}{1 + r^2}\left(\frac{D_i}{N_i}\frac{dN_i}{dy}\right) - \frac{\cos I \sin I}{1 + r^2}\left(\frac{D_i}{N_i}\frac{dN_i}{dz} + \frac{k}{m_i \nu_{in}}\frac{dT}{dz}\right), \tag{6}$$

where $D_i = \frac{kT_i}{m_i \nu_{in}}$ is the ion diffusion coefficient. T_i is the ion temperature obtained from the International Reference Ionosphere-2012 (IRI-2012; Bilitza et al., 2014). k is Boltzmann's constant, and $r = \frac{m_i \nu_{in}}{eB_0}$ is the ratio between the ion-neutral collision frequency and the gyro-frequency. Here we ignore the temperature gradient in the meridional direction because the vertical gradient of temperature is much larger than the horizontal gradient (Kelly, 2009; Schunk & Nagy, 2009).

For the ion velocity components due to the electric field perpendicular to $\vec{B}$,

$$V_{izE\perp B} = \frac{E_{\perp x}\cos I}{(1+r^2)B_0} + \frac{rE_{\perp z}}{(1+r^2)B_0}, \tag{7}$$

$$V_{iyE\perp B} = \frac{E_{\perp x}\sin I}{(1+r^2)B_0} + \frac{rE_{\perp y}}{(1+r^2)B_0}. \tag{8}$$

The first term on the right-hand side of equations (7) and (8) are the z and y components of the $\vec{E}\times\vec{B}$ drift, respectively. The second terms are the z and y components of the Coulomb-induced drift along the $\vec{E}_{\perp}$ direction.

The ambipolar diffusion terms are given by.

$$V_{izE//B} = \frac{e}{m_i v_{in}} \frac{\vec{E}_{//}\bullet\vec{B}}{B_0(1+r^2)}\sin I, \tag{9}$$

$$V_{iyE//B} = \frac{e}{m_i v_{in}} \frac{\vec{E}_{//}\bullet\vec{B}}{B_0(1+r^2)}\cos I. \tag{10}$$

We obtain $\vec{E}_{//}$ from the electron-momentum equation. By ignoring all terms with the mass of an electron and projecting the equation parallel to $\vec{B}$ to remove the terms of electron velocity cross $\vec{B}$ (Schunk & Nagy, 2009), we obtain.

$$\vec{E}_{//} = -\frac{1}{eN_e}\vec{\nabla}//p_e, \tag{11}$$

where $\vec{\nabla}//p_e$ is the gradient of electron pressure parallel to $\vec{B}$. Here we project $\vec{\nabla}//p_e$ into z and y directions and then equations (9) and (10) can be written as.

$$V_{izE//B} = \frac{e}{m_i v_{in}} \frac{E_{//y}\cos I + E_{//z}\sin I}{(1+r^2)}, \tag{12}$$

$$V_{iyE//B} = \frac{e}{m_i v_{in}} \frac{E_{//y}\cos I + E_{//z}\sin I}{(1+r^2)}. \tag{13}$$

where $E_{//z} = -\frac{kT_e}{eN_e}\frac{dN_e}{dz} - \frac{k}{e}\frac{dT_e}{dz}$ and $E_{//y} = -\frac{kT_e}{eN_e}\frac{dN_e}{dy}$. Again, as we did for ion temperature, we use the electron temperature, T_e from IRI-2012, and ignore the meridional gradient of T_e. We assume quasi-neutrality, so the electron number density (N_e) is equal to the sum of all ion number densities (such as NO^+, $O_2{}^+$, and Na^+).

For the ion velocity components due to neutral winds:

$$V_{izu} = \frac{Ur\cos I + V\cos I\sin I + W\left(r^2 + \sin^2 I\right)}{1+r^2}, \tag{14}$$

$$V_{iyu} = \frac{V(r^2 + \cos^2 I) + W\cos I\sin I - Ur\sin I}{1+r^2}. \tag{15}$$

For the ion velocity components due to gravity:

$$V_{izg} = \frac{g(z)\left(r^2 + \sin^2 I\right)}{v_{in}(1+r^2)}, \tag{16}$$

$$V_{iyg} = \frac{g(z)(r^2 + \sin I\cos I)}{v_{in}(1+r^2)}. \tag{17}$$

Here the term $g(z)$ is the z component of gravity and it is height dependent. Equation (17) is the crucial part of the fountain effect in the equatorial ionosphere, which is the phenomenon that ions are transported

upward at the geomagnetic equator due to the upward $\vec{E}\times\vec{B}$ drift in the daytime, and subsequently, move downward and away from the geomagnetic equator due to gravity and diffusion in the nighttime.

Apart from above terms mentioned that can be directly solved from equation (2), eddy diffusion is also very important for transport, especially below the turbopause (Plane, 2004). Therefore, it must also be included in our model and is artificially added to equations (3) and (4), as was done in Cai et al. (2017).

The ion transport velocity components due to eddy diffusion are.

$$V_{ized} = -k_{zz}\left(\frac{1}{H}+\frac{1}{T_n}\frac{\partial T_n}{\partial z}+\frac{1}{N_i}\frac{\partial N_i}{\partial z}\right), \tag{18}$$

$$V_{iyed} = -k_{zz}\left(\frac{1}{H}+\frac{1}{T_n}\frac{\partial N_i}{\partial y}\right), \tag{19}$$

where k_{zz} is the eddy diffusion coefficient and it is adopted from WACCM-Na (Marsh et al., 2013). $H=\frac{kT_g}{mg}$ is the scale height. T_n is the neutral temperature and m is the average mass of air. Equations (18) and (19) are added to equations (3) and (4), respectively. Above the turbopause, the eddy diffusion coefficient decreases rapidly and, for altitudes above 140 km (upper limit of WACCM-Na), we set it to zero. In addition, by comparing the eddy diffusion coefficient with ion diffusion coefficient, we find that the latter is much larger (10^3 to 10^4 m^2/s) than the former (10^1 to 10^2 m^2/s) between 110 to 140 km, with the differences increasing with the increasing of altitude because the ion diffusion coefficient increases while the eddy diffusion coefficient decreases.

2.1.2. Transport of Neutrals

Following equation (10.51) in Schunk and Nagy (2009), we construct the neutral transport velocity components in the z and y directions, which include contributions from neutral winds, gravity, eddy diffusion, and molecular diffusion. The vertical and meridional transport equations are.

$$V_{nz} = W-k_{zz}\left(\frac{1}{H}+\frac{1}{T_n}\frac{\partial T_n}{\partial z}+\frac{1}{N_n}\frac{\partial N_n}{\partial z}\right)-D_n\left(\frac{1}{H_n}+\frac{1}{T_n}\frac{\partial T_n}{\partial z}+\frac{1}{N_n}\frac{\partial N_n}{\partial z}\right)-\frac{g(z)}{\nu_{nn}}, \tag{20}$$

$$V_{ny} = W-k_{zz}\left(\frac{1}{H}+\frac{1}{N_n}\frac{\partial N_n}{\partial y}\right)-D_n\left(\frac{1}{H_n}+\frac{1}{N_n}\frac{\partial N_n}{\partial y}\right). \tag{21}$$

The neutral transport velocity components also can be separated into two groups, as well. One is the neutral velocity, which is the sum of neutral wind (W in vertical and V in meridional directions) and gravity term (only in the vertical direction). Another group is neutral diffusion, which is the sum of eddy and molecular diffusion. Molecular diffusion (D_n) dominates above the turbopause, and we follow Banks and Kocharts (1973) to calculate D_n (the details can be found in Cai et al. (2017)). $H_n=\frac{kT_n}{m_n g}$ is the scale height of the neutral species n, and m_n is the mass of this species. Similar to the ion diffusion coefficient, the molecular diffusion coefficient also increases rapidly above 110 km, and the effect of eddy diffusion in equations (20) and (21) decreases quickly above 110 km.

2.2. Models Providing Neutral Atmospheric Parameters

In the E and lower F region (120–200 km), there are very few observations of neutral temperature and winds, except for some sparse lidar observations. However, in most cases, the number density of metals (120–200 km) are much weaker compared to the main metal layers, making it difficult to extract the robust and continuous temperature and wind as is done in the altitude range (80–105 km) of the main metal layer. Therefore, we have to utilize models to provide the neutral atmosphere environment to study variations of Na and Na^+. We use the data assimilation version of the Whole Atmosphere Community Climate Model eXtended (WACCMX) and Climatological Tide Model of Thermosphere (CTMT). WACCMX-DART incorporates data assimilation by using the Data Assimilation Research Testbed (DART) ensemble Kalman filter. By incorporating data assimilation, WACCMX-DART provides a relatively realistic depiction of the atmospheric state (Pedatella et al., 2014, 2018). The spatial resolution of WACCMX-DART is 1.9° and 2.5° in the meridional and zonal directions, respectively, which is consistent with the meridional resolution

of our model at 1.9°. The WACCMX-DART simulations used in the present study include realistic solar and geomagnetic forcing, which are parameterized by $F_{10.7}$ and *Kp*, respectively. The WACCMX-DART simulations were performed using an identical setup as in Pedatella et al. (2018), and similarly use a 40-member ensemble and assimilate conventional meteorological observations as well as Aura Microwave Limb Sounder (MLS) and Thermosphere Ionosphere Mesosphere Energetics and Dynamics (TIMED) satellite Sounding of the Sounding of the Atmosphere using Broadband Emission Radiometry (SABER) temperatures.

In addition, many previous studies (Forbes et al., 2008, 2014) suggest that atmospheric tides strongly influence the atmospheric dynamics between 110 and 200 km. Thus, the specification of tides in this region may help us uncover the mechanisms of TSL formation. The CTMT is a climatological tidal model (semidiurnal and diurnal tide) developed by Oberheide et al. (2011) based on the measured temperatures and winds (below 110 km) from the TIMED satellite. The tides in CTMT are extended vertically using Hough Mode Extensions up to 400 km (Oberheide et al., 2011). The CTMT resolution is 5° in latitude (longitude information is determined by external input). Its results have already been compared with lidar measurements below 110 km. Although the phase outputs match well with lidar measurements (Yuan et al., 2014), the tidal amplitudes are mostly underestimated in CTMT (Häusler et al., 2015). Note that the WACCMX-DART upper limit is 452 km and CTMT is 400 km, which are lower than our model upper boundary (490 km). According to Wang et al. (2008), during geomagnetically quiet times, the viscosity in the upper thermosphere smooths out the vertical gradient of horizontal winds in low and middle latitudes above 250 km. The neutral temperature above 400 km in WACCMX-DART is almost constant with altitude, as well. Therefore, we set the neutral parameters at altitudes above WACCMX-DART and CTMT upper boundaries to the same values as their upper boundaries.

3. Results and Discussions

3.1. Observation of TSLs at ALO

By checking the TSL events from 154 nights of lidar observations between May 2014 and January 2018 (Table 1) at ALO, we find 23 nights with TSL events. As shown by Liu et al. (2016) and Gardner (2004), the Na lidar system sensitivity or the minimum detectable number density of a species (Na) that is able to be observed varies with different resolutions. The temporal and spatial resolutions of the ALO observations are 0.5 km and 1 min. At this resolution, and the background noise at ALO, Na densities above 0.5/cm^3 can be detected. Note that we focus on those TSLs with obvious dynamic features. These selected TSLs are all exhibit descending features, namely, the time and altitude distributions of Na number density showing a downward phase progression. Of the observed 23 TSLs, 12 TSLs occurred during spring equinox (March and April) and 7 occurred during fall equinox (September and October), which suggests that the TSLs mainly appear during the equinox. In addition, 22 out of 23 TSLs appear during the second half of the night and continue to the end of the night. These consistent features indicate that we can study the TSL formation using a climatological model.

An example of the TSL (23 April 2015) observed by ALO is shown in Figure 1. In this case, the sodium density data are further averaged to lower resolution (1 hr in time and 2 km in altitude) to reduce the uncertainty of the observed sodium density to less than 0.1/cm^3 so that the TSL can be better identified. The 1-hr data are then interpolated into 10-min resolution. It is worth noting that there are 10 TSLs observed in April, making it the month with the greatest number of observed TSLs at ALO. Most of these TSLs show obvious downward phase progression, allowing the estimation of the speed. To estimate the speed, we first identify the maximum density at each altitude (between 120 and 170 km), as shown in Figure 1. By checking the ratio of the corresponding error to maximum measured Na density, we find that the ratio increases with higher altitude as expected, reaching a maximum of less than 9% (not shown here). A second-order polynomial fit in altitude time of these peak value locations is performed and the results along with the errors (*R* square is 96.7%) are shown as the magenta line in Figure 1. The results indicate a downward phase progression with increasing vertical phase speed at higher altitudes. The average downward phase progression speed is estimated to be 10.5 $\pm$ 1.5 km/hr, which is similar to the previously reported 11–12-km/hr downward phase progression of TSLs (Gao et al., 2015), and 9.2 km/hr for the thermospheric K layer (Friedman et al., 2013). It is

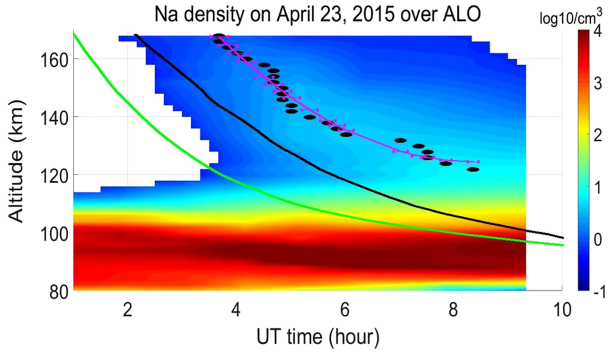

Figure 1. Thermospheric Na layer observed over ALO, Chile on 23 April 2015. The black line is the phase line of the density modulation of semidiurnal tide and the green line is the phase line of vertical wind modulation of semidiurnal tide from CTMT. The pink line is the phase line from the fitted number density maxima in each altitude and the fitting error. White part is the area where Na number density is less than 0.5/cm^3.

clearly illustrated in Figure 1 that the uncertainty in the phase estimation due to the uncertainty of density measurement is very small, less than 0.1 hr over the 4-hr period, or 2.5%.

Figure 1 also depicts the phase lines of the modulation of the vertical wind and atmospheric density by the semidiurnal tide at ALO from CTMT. The phase line of tidal density modulations (black line) leads the fitted phase line of the number density of TSL (magenta line) by 1.4 to 2.2 hr, which is less than a quarter of the period of semidiurnal tide and within the day-to-day tidal phase variability (Yuan et al., 2010). The TSL follows well with the atmospheric density modulations generated by the semidiurnal tide, indicating that its formation can be closely associated with the semidiurnal tide. In addition, the vertical wind modulations of the semidiurnal tide in April at ALO from CTMT (not shown here) reveals the possible existence of a region for Na accumulation (downward wind above and upward wind below) also occurring during the second half of the night. This may be the reason why most of the TSLs at ALO are observed during the second half of the night. Furthermore, the seasonal variations of the semidiurnal tide in CTMT reveal that the maximum amplitudes in density modulation occur during April at ALO.

Thus, the TSLs at ALO appear to be related to the semidiurnal tide. In addition, ALO is located at low geomagnetic latitude (20°S), and therefore, the electric field and the fountain effect can also influence the motion of Na^+, which may also affect distribution of Na indirectly. To isolate different factors on forming the TSL, we have performed four simulations. In the first simulation, we run the extended 2-D model driven directly with the neutral atmosphere outputs of the high-resolution WACCMX-DART and the electric field from Eccles (1998) to see how Na and Na^+ vary at ALO. The date of the output of WACCMX-DART is from 22 to 23 April 2015 because we want to see whether the observed TSL on 23 April 2015 can be formed with the same day output of WACCMX-DART. The reason to include 22 April is because our model needs one day to reach equilibrium so that the initial conditions cannot influence the output. Then the model can solve the variations of Na and Na^+ self-consistently. The $F_{10.7}$ is 150 solar flux unit (sfu) and it is geomagnetic quiet time. In the second run, we utilize the 24-hr means of WACCMX-DART combined with tidal outputs from CTMT in April to form a new hybrid neutral atmosphere and the same electric field used in the first simulation to drive our model in order to investigate specifically how tidal waves can influence the distributions of Na and Na^+. In the third simulation, still driven by WACCMX-DART on 23 April 2015 and the electric field from Eccles (1998), we aim to examine the influence of fountain effect on the distributions of Na^+ and Na by removing the electric field perpendicular to $\overrightarrow{B}$. Finally, in the fourth simulation, still utilizing WACCMX-DART, we study the contributions of vertical and horizontal transports individually on the variations of Na and Na^+. Based on the results obtained from these four simulations, we try to understand the mechanism of TSL formation at ALO and reproduce a similar structure.

3.2. Results From WACCMX-DART

Figure 2 shows the temporal variations of the simulated vertical height profiles of vertical ion velocity ($V_{iz\perp B} + V_{izu} + V_{izg}$), vertical neutral velocity ($W - \frac{g(z)}{\nu_{nn}}$), and number densities of Na^+ and Na at ALO between 90

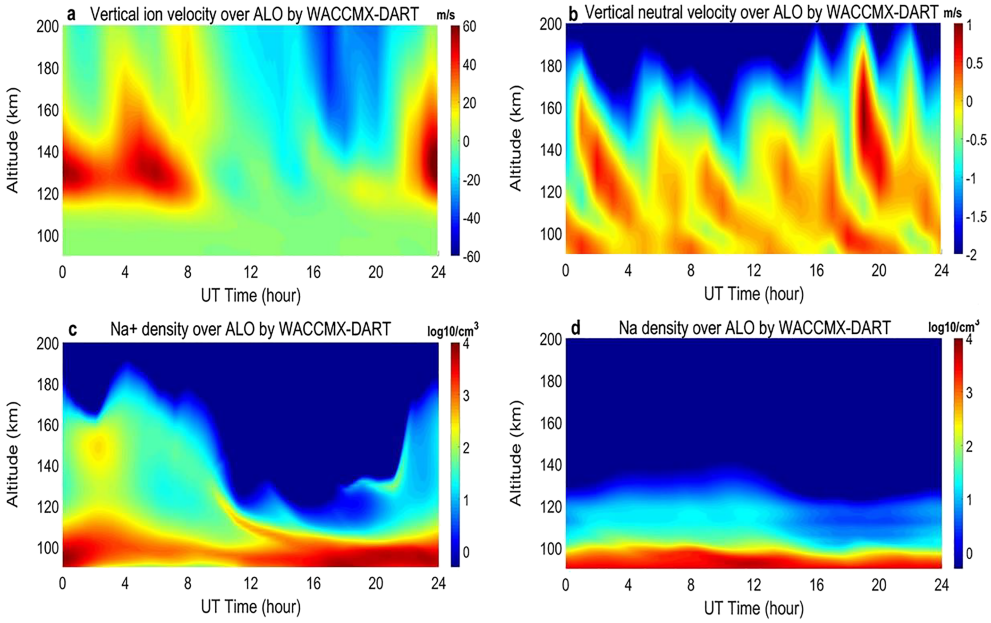

Figure 2. Time and altitude distribution of a vertical ion velocity, b vertical neutral velocity, c number density of Na^+, and d Na over ALO by WACCMX-DART. The daytime is from 11:05 UT to 22:10 UT, and nighttime is from 22:10 UT to 11:05 UT.

and 200 km for 0 to 24 UT on 23 April 2015. To compare with the observed Na number density at ALO (the data can be found at http://lidar.erau.edu/data/nalidar/index.php), we set the densities of Na and Na^+ into log scale (base 10) with maximum 4 and minimum −0.3, which corresponds to the Na density range observed at ALO (0.5–10,000/cm^3 from the above link). The number densities of Na and Na^+ above 200 km are not shown because both of them are less than 0.5/cm^3. Regarding the vertical ion and neutral velocities, vertical ion velocity in Figure 2a has maximum 60 m/s, while vertical neutral velocity (Figure 2b) is much smaller (only −10 to 1 m/s).

The diurnal variation of Na^+ is shown in Figure 2c. Note that the nighttime is from 0:00 UT to 11:00 UT and 22:00 UT to 24:00 UT, and the daytime is from 11:00 UT to 22:00 UT. The topside of the Na^+ layer extends to 190 km at night, reaching a maximum altitude at 4:00 UT. The height of the topside decreases after it reaches this peak altitude until daytime (11:00 UT) approaches. During the daytime, the topside of the Na^+ layer only extends up to a maximum of 130 km. After sunset (~22:00 UT), the top of the Na^+ layer starts to increase in height until it again reaches 180 km within the first 1 to 2 hr of the night. By comparing the vertical ion velocity in Figure 2a with the variations of the topside of the Na^+ layer in Figure 2c, we find that the Na^+ variations are closely correlated with the vertical ion velocity. For convenience of discussion, we present the electric field perpendicular to $\vec{B}$, and the corresponding vertical ion velocity due to $\vec{E}\times\vec{B}$ drift, Coulomb-induced drift, and neutral winds in Figure 3. For vertical ion velocity, the z component of $\vec{E}\times\vec{B}$ drift and Coulomb-induced drift are mainly determined by $E_{\perp x}$ and $E_{\perp z}$. Figure 3a depicts that $E_{\perp z}$ (green line) reaches its peak value (2.37 mV/m) between 1:00 UT and 1:45 UT and decreases and changes direction to downward after 11:00 UT. From equation (7), the vertical component of $\vec{E}\times\vec{B}$ drift increases with altitude until $r \to 0$ (around 250 km). The vertical component of Coulomb-induced drift maximizes when $r \approx 1$ (around 130 km), and then decreases with altitude due to the decrease of r. Figure 3b shows that the vertical component of $\vec{E}\times\vec{B}$ drift is around −20 m/s above 130 km before 11:00 UT. The vertical component of Coulomb-induced drift in Figure 3c has a maximum value of 50 m/s at 130 km between 1:00 UT and 1:45 UT, and then decreases to almost 0 m/s at 11:00 UT. The sum of the vertical ion velocity before 11:00 UT due to the electric field perpendicular to $\vec{B}$ will form a region with downward vertical ion velocity above 152 km and upward below 152 km until 6:50 UT. These effects tend to form an accumulation of ions near 150 km. However, the vertical ion velocity due to the neutral wind (Figure 3d) is 18–22 m/s above 130 km

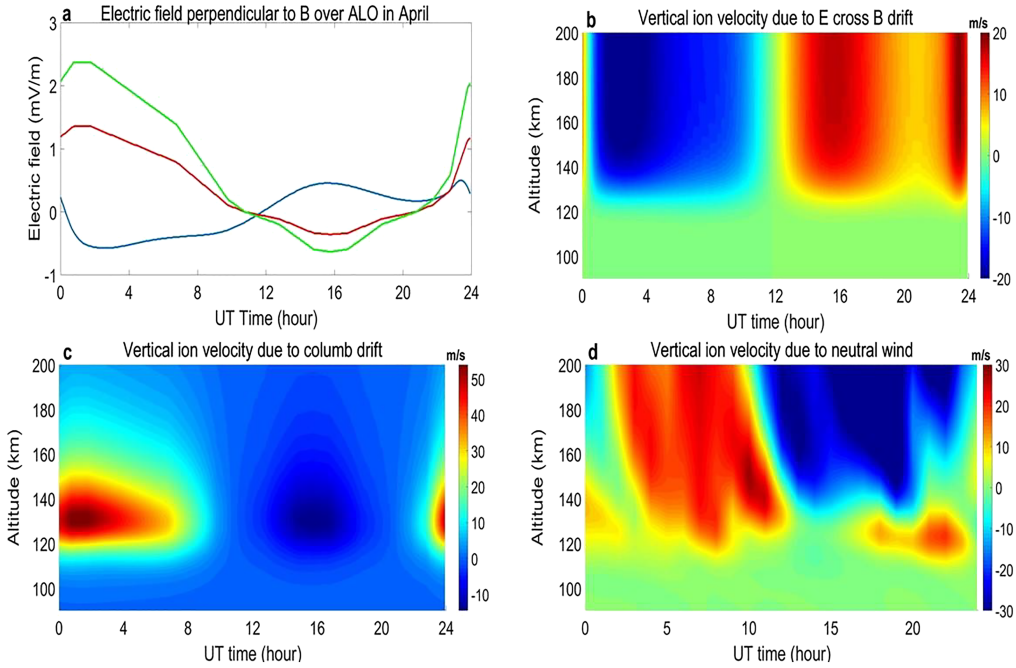

Figure 3. The x (blue), y (red), and z (green) component of the electric field perpendicular to B over ALO in April quiet time. The vertical ion velocity due to (b) $\vec{E}\times\vec{B}$ drift, (c) coulomb-induced drift, and (d) neutral wind.

before 11:00 UT. The ion accumulation region will therefore decrease with the inclusion of vertical ion velocity due to the neutral wind. Due to the combined effects of the influences described above, a region of Na^+ densities around $10^{2.5} = 315/cm^3$ is formed between 140 and 160 km before 4:00 UT (Figure 2c).

During the daytime, $E_{\perp z}$ is downward, causing a downward vertical component of Coulomb-induced drift (peak value −14 m/s), $E_{\perp x}$ is eastward and generates a 17 to 20-m/s vertical component of $\vec{E}\times\vec{B}$ drift above 130 km. The vertical ion velocity due to neutral wind is −30 to −40 m/s above 120 km during the daytime. Therefore, the total vertical ion velocity is negative above 130 km, pushing ions downward and resulting in the topside of the Na^+ layer being located at 130 km during the daytime. After 18:00 UT, $E_{\perp z}$ begins to change direction to upward and its value increases. In addition, there appears a region of upward vertical ion velocity due to the neutral winds and it expands after 18:00 UT. Thus, regions of ion accumulations are expanded and finally, the topside of Na^+ layer extends to 180 km at 24:00 UT. The discussion above reveals that the vertical ion velocity due to electric field perpendicular to $\vec{B}$ mainly acts to accumulate ions at night, while it works together with the vertical ion velocity due to neutral winds to prevent ion accumulation above 130 km during daytime at ALO.

Turning to the density variations of Na (Figure 2d), the topside of the Na layer tends to move upward during the night. At the beginning of the night, the density of Na is $10/cm^3$ at 110 km. At the end of the night (11:00 UT), the density of Na at 110 km increases to $10^{1.4} = 25/cm^3$, and altitude where the density is $10/cm^3$ increases to 120 km compared with 110 km at the beginning of the night. The height of the topside of the layer decreases during the day as a result of the increase of photo-ionization. The increase of solar radiation also triggers the increase of NO^+ and $O_2{}^+$ during the daytime, which further enhances the Na ionization reactions. When dusk approaches, the layer begins to extend to higher altitudes. Near the end of the day, two small peaks above 100 km become a bit more prominent. One is around 105 km and another at 118 km. This is mainly attributed to the effect of the source function (see Figure 2b in Cai et al. (2017)), which has two peaks at 105 and 118 km, respectively. Unlike Na^+, the variations of Na are not well correlated with the vertical neutral velocity (Figure 2b). There are several 2–4-hr fluctuations in vertical neutral velocity, but they do not generate corresponding variations in Na density. This is due to the increase of molecular diffusion coefficient above 120 km, which makes it very difficult for the accumulation of Na. In addition, the influence of the gravity term in equation (20) makes the downward vertical neutral velocity increase with

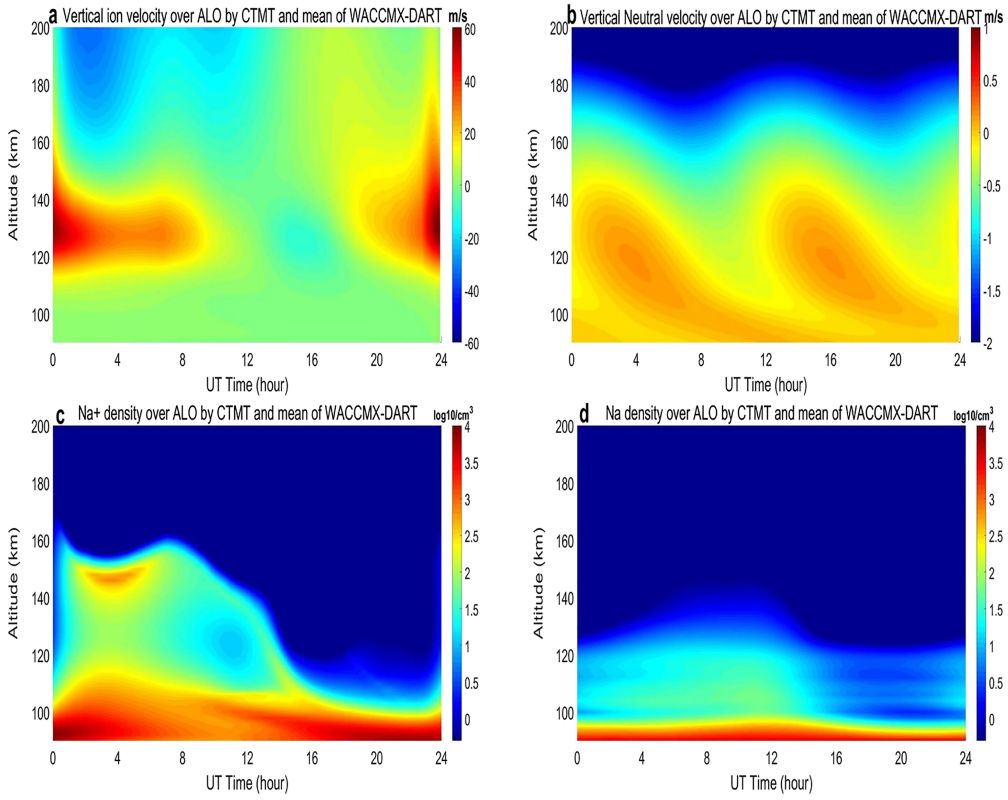

Figure 4. Time and altitude distributions of a vertical ion velocity, b vertical neutral velocity, c number density of Na^+, and d Na over ALO by the hybrid model of 24-hr WACCMX-DART mean and CTMT.

altitude, which enhances the downward transport of Na and further prevents Na from accumulating like Na^+ (an example is the Na^+ layer around 150 km before 4:00 UT shown in Figure 2c). Overall, the simulation driven directly by WACCMX-DART does not generate the lidar observed TSLs naturally, possibly due to the imperfect description of neutral dynamic condition in the *E* region or some particular dynamic condition needed for TSL formation. In the following section, we investigate how Na and Na^+ vary by performing the simulation with the mean of WACCMX-DART together with the CTMT.

3.3. Results From the Combination of CTMT and the Mean Field From WACCMX-DART

Figure 4 shows the vertical ion velocity ($V_{iz\perp E} + V_{izu} + V_{izg}$), vertical neutral velocity ($W - \frac{g(z)}{\nu_{nn}}$), Na and Na^+ density variations for the simulation with the neutral atmosphere specified with CTMT tides, and WACCMX-DART diurnal means. Regarding the Na^+, the region of Na^+ accumulation is around 150 km and lasts longer (until 6:00 UT) than that in the previous simulation (until 4:00 UT; see Figure 2c). Unlike the Na^+ with the full neutral atmosphere from WACCMX-DART, the topside of Na^+ in Figure 4c does not reach up to 190 km, but stays below 160 km. As dawn approaches, the topside of the layer descends 40–60 km, which is similar to Figure 2c. In addition, the Na^+ number density in this simulation is less than the Na^+ in the first simulation after 21:00 UT, and the Na^+ layer descends downward to almost 130 km. Most of these differences can be attributed to different model resolutions and configurations. Furthermore, CTMT only includes semidiurnal and diurnal tides, while WACCMX-DART includes not only tides but also gravity waves and other sources of variability such as planetary waves. Therefore, it is not surprising that the outputs of WACCMX-DART and CTMT are different, and that they generate different ion velocities and neutral velocities to form different distributions of Na and Na^+. Regarding the Na density (Figure 4d), it also exhibits an extended layer during the nighttime and a decrease in the layer topside during the daytime. Compared with the Na density in the simulation driven purely by WACCMX-DART, there are insignificant differences in the Na number density. For example, the Na number densities at 120 km around 11:00 UT are 16/cm^3 for

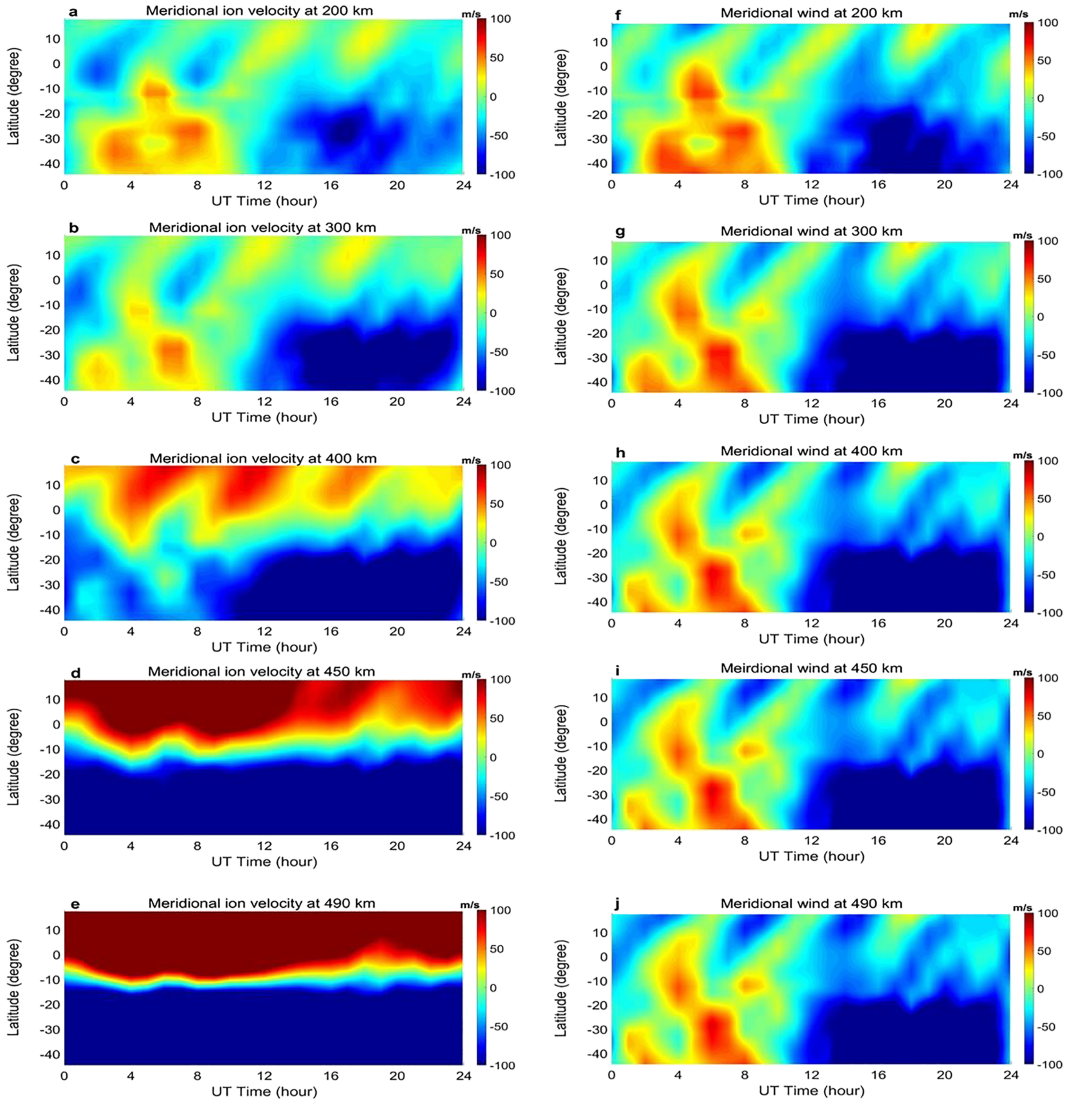

Figure 5. Time and latitude distributions of meridional ion velocity of Na^+ at a 200 km, b 300 km, c 400 km, d 450 km, and e 490 km, and (f–j) the corresponding meridional winds.

WACCMX-DART and 19/cm^3 for CTMT. Na densities obtained from both simulations show an increase from the beginning of the night to the beginning of the day (from 6.6/cm^3 at 120 km (0:00 UT) to 16/cm^3 at 120 km (11:00 UT) using WACCMX-DART, and from 6/cm^3 at 120 km (0:00 UT) to 19/cm^3 at 120 km (11:00 UT) using CTMT). This is also in agreement with the observations depicted in Figure 1, which shows that the topside of the main layer moves up from 115 km at the beginning of the night to above 120 km by the end of the night. And the Na number density at 120 km increase from less than 0.5 to 6.3/cm^3. Again, the change of Na is not well correlated to the variations of vertical neutral velocity driven by standard tidal amplitude output. Overall, the second simulation (driven by the diurnal mean of WACCMX-DART combined with CTMT) demonstrates that the TSLs cannot be formed using the standard climatological tidal amplitudes from CTMT, either.

3.4. Fountain Effect

The discussion in section 3.2 indicates that Na^+ is mainly confined below ~ 200 km at ALO. Our simulations also show that only the locations near the geomagnetic equator (12°S at 71°W; not depicted here) can have some Na^+ distributed up to 300 km (<100/cm^3). Thus, it is possible that the fountain effect first lifts Na^+ to a

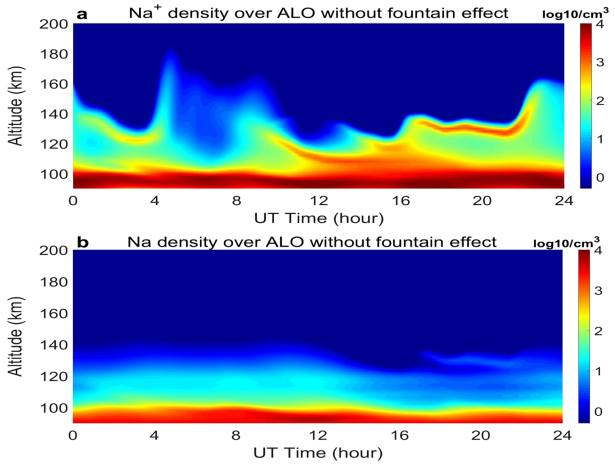

Figure 6. Time and altitude distributions of (a) Na^+ and (b) Na over ALO without fountain effect.

higher altitude during the daytime above the geomagnetic equator, and then the Na^+ diffuses down along the field lines to the subtropical *E* and lower *F* region on both sides of the geomagnetic equator. Before we investigate the fountain effect contributions using the model driven by WACCMX-DART and electric field from Eccles (1998); we first discuss the meridional ion velocity and meridional wind in the thermosphere that are critical for the fountain effect. The left column in Figure 5 depicts the meridional ion velocity of Na^+ generated by WACCMX-DART at 200, 300, 400, 450 and 490 km and the corresponding meridional winds are presented in the right column. It clearly illustrates that the meridional wind dominates the meridional ion velocity up to 300 km. Differences between the meridional ion velocity and meridional wind become apparent near and above 400 km. However, the meridional ion velocity driven by gravity (equation (17)) increases exponentially with altitude due to the exponential decrease of the ion-neutral collision frequency, and dominates over all other terms in the meridional ion velocity at high altitudes. At 450 and 490 km, the meridional ion velocities are northward in the north of the geomagnetic equator and southward in the south, meaning that ions can be transported to both sides of the geomagnetic equator. It should be noted that the above description is for the fountain effect during the nighttime.

Previous studies, such as Gao et al. (2015), proposed a hypothesis that the TSL might be generated from the recombination between Na^+ and electrons. They assumed that Na^+ is lifted upward during the daytime near the geomagnetic equator and then transported by gravity and diffusion to both sides of the geomagnetic equator at night, and it took 2 hr to form a Na layer with $6/cm^3$ from a rough estimation (500-K neutral temperature, $4{,}400/cm^3$ Na^+, and $10^5/cm^3$ electron density). To test this hypothesis, we run our extended 2-D model again without the fountain effect by setting the electric field perpendicular to $\vec{B}$ to zero. This removes the upward ion transport at the geomagnetic equator, which is a prerequisite for the fountain effect. We keep the gravity term because it changes little during the quiet time while the electric fields are different on a daily basis. The other neutral parameters are specified by the full WACCMX-DART fields. The resulting Na^+ and Na densities are shown in Figure 6. By comparing them with Figure 2, we find that the topside of Na^+ layer before 4:00 UT decreases in altitude to below 140 km without this electric field component and the density is lower at night. This again demonstrates that this region of Na^+ accumulation is mainly generated by the electric field perpendicular to $\vec{B}$. On the other hand, there is an elevated Na^+ layer during the daytime after 16:00 UT. Around 130 km, the Na^+ density is only $10^{1.8}/cm^3$ from 17:00 UT to 21:00 UT when the electric field perpendicular to $\vec{B}$ is included (Figure 2c). This region expands for a longer time (16:00 UT–22:30 UT) with a higher density of Na^+ (peak density $10^{3.2}/cm^3$) when the electric field is removed from the simulation (Figure 6a). As for Na density (Figure 6b), it is similar to Figure 2d during the nighttime. However, there are some distinct Na variations in the daytime when the fountain effect is not included. After 17:00 UT, there appears a sharp Na layer with peak density $10^{0.5}/cm^3$ around 130 km and width of ~5 km, which lasts until 22:30 UT. This layer is due to the strong Na^+ layer near the same altitude during this time. With a strong Na^+ layer (peak density $10^{3.2}/cm^3$) continuing for several hours, the recombination reaction between Na^+ and electrons becomes vital for the generation of Na during the daytime, which results in the Na layer with peak density of $10^{0.5}/cm^3$.

The above comparison indicates that vertical components of $\vec{E}\times\vec{B}$ drift and Coulomb-induced drift due to the electric field perpendicular to $\vec{B}$ play significant roles in the formation of the nighttime Na^+ between 120 and 200 km at ALO, while they decrease Na^+ density during the daytime. However, the fountain effect is found to have little effect on the variations of Na during nighttime. In addition, as we mentioned earlier, the meridional ion velocity is only dominated by gravity-driven ion motion along the field lines above 400 km, where Na^+ density is extremely low (only existed up to 300 km at geomagnetic equator with a density less than $100/cm^3$). Thus, there is not enough Na^+ that is able to reach the altitudes where the gravity-

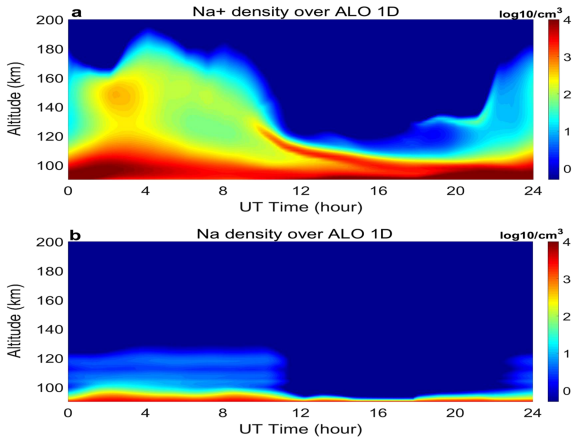

Figure 7. Time and altitude distributions of (a) Na^+ and (b) Na over ALO with only vertical transport.

driven ion motion dominates and transports ions to low geomagnetic latitude regions. Therefore, we can conclude that the formation of TSL at ALO has little contribution from the fountain effect.

3.5. Vertical and Horizontal Dynamic Transports

With the current WACCMX-DART 2-D results (shown in Figure 2), we can remove the horizontal transport and only run the model with vertical transport (becoming 1-D simulation) to study their contributions individually. The results of this experiment are shown in Figure 7. Na^+ variations in Figure 7a are similar to those based on the full extended 2-D model (Figure 2c). The only difference is the larger peak density of Na^+. Na^+ in the full 2-D simulation has a peak density of around $10^{3.9}/cm^3$, while the Na^+ obtained without horizontal transport is $10^{4.3}/cm^3$. As for the Na^+ layer around 150 km, the peak density in the 2-D model is $10^{2.5}/cm^3$, while the density increases slightly to $10^{2.6}/cm^3$ in the simulation with only vertical transport. This once again demonstrates that the distribution of Na^+ in the ionosphere E and lower F region (120–200 km) is mainly determined by the vertical transport caused by vertical ion velocity. Although the horizontal transport can diffuse the accumulated Na^+, it is unable to alter the overall structure of the Na^+ layer significantly. It should be noted that with the increase of altitude, ion diffusion and ambipolar diffusion coefficients also increase rapidly. They generate large diffusion terms that contribute significantly to the ion diffusion process, leaving the vertical ion velocity as the most probable factor controlling the ion accumulation in the altitude range below 200 km. Note that below 200 km, the gravity term (equation (16)) at ALO is at most around −0.5 m/s, which is considerably less than the vertical ion velocity (with maximum 60 m/s). Therefore, the vertical ion velocity is primarily due to $V_{izE\perp B}$ and V_{izu}, and these terms will mainly control the structure of Na^+ layer below 200 km.

Figure 7b shows the variation of Na in the simulations with only vertical transport included. The number density exhibits clear diurnal variations. The topside of the Na layer decreases (from 120 to below 105 km) after sunrise (11:05 UT) and increases (again to 120 km) after sunset (22:10 UT). The Na density above 100 km diminishes quickly after sunrise when it drops to $10^{-0.5}/cm^3$ in the daytime, much lower compared to the results of the full 2-D simulation ($10^{1.2}$–$10^{1.8}/cm^3$). This suggests that the horizontal transport increases the number density of Na during the daytime below 120 km but does not significantly influence the formation of the descending layer feature.

Through examining the individual terms of the neutral transport velocity in equation (20), we are able to explain the major features seen in the Na variations. Note that the observed TSLs exhibit the features that a certain amount of Na is collected between 120 and 170 km during the second half of the night. The only possible term to accumulate Na is the vertical neutral velocity, namely, the sum of vertical wind (W) and the gravity term. Unlike equation (16), which is a mere −0.5 m/s at 200 km in vertical ion velocity, the absolute value of the gravity term in equation (20) for the vertical neutral velocity is much larger (−10 m/s at 200 km and − 3.6 m/s at 170 km). Furthermore, the gravity term of the vertical neutral velocity only transports neutrals downward. Thus, the only probable term to transport neutrals upward in the E and lower F region is the vertical wind (W), which has to be large enough to compensate for the gravity term. This vertical wind (W) consists of a mean field and vertical wind perturbations, which include tidal wave modulation, gravity wave modulation, and other unknown dynamic vertical perturbations (modulation refers those from the known sources while perturbation refers to those from the unknown sources). The mean field is very small in the E and lower F region (<0.1 m/s, from WACCMX-DART results). Thus, vertical wind perturbations are needed in order for the vertical wind to dominate over the gravity and diffusion terms to move the species upward. By checking the current simulations, the vertical wind perturbations provided by WACCMX-DART are between −2 and 1 m/s below 200 km. The amplitude of the climatological tidal vertical wind modulation from CTMT is even smaller (0.3-m/s maximum) at ALO. Both of them cannot dominate over the gravity term. In other words, current standard model predictions of vertical wind modulations are too small to transport a considerable amount of Na upward into altitudes above 120 km.

Therefore, based on the simulation results and the discussions so far, a large vertical neutral transport (equation (20)) generated by large vertical wind perturbations that are able to compensate for the effects of diffusion and gravity terms is needed to form a TSL. Chu and Yu (2017) utilized gravity waves with large vertical wind modulations (12 m/s at 150 km) in their simulations and successfully reproduced the observed wave feature of the thermospheric Fe layer over McMurdo, Antarctica. This amplitude is large enough to compensate for the molecular diffusion and the horizontal wind divergence. Indeed, while the WACCMX-DART and CTMT models do not generate vertical wind perturbation of this magnitude, there are many observations of large vertical wind perturbations in the lower thermosphere that lasted more than 1 hr. For example, Larsen and Meriwether (2012) provided a summary of the large vertical wind perturbations measurements covering low, middle, and high latitudes. Their work summarizes the amplitude of the vertical wind perturbations in the *E* and *F* region ranging from slightly less than 10 to 50 m/s.

3.6. The Proposed Mechanism for TSL

Based on our simulations, we conclude that the recombination reaction between Na^+ and electrons, fountain effect, and horizontal transport do not significantly contribute to the generation of the TSL. The possibility of the source function contribution can also be removed because there is little meteoroid ablation above 120 km (Vondrak et al., 2008). Therefore, a likely factor to generate the TSL is the large vertical neutral transport (equation (20)) generated by large vertical wind perturbations. As we mentioned earlier in section 2.1.2, the vertical neutral transport velocity (equation (20)) consists of vertical neutral velocity and vertical neutral diffusion. The vertical neutral velocity has contributions from the vertical wind (W) and gravity term ($\frac{g(z)}{\nu_{nn}}$). As for the vertical wind, it is the combination of the mean field and vertical wind perturbations. The total vertical wind perturbation consists of several components as follows:

$$w' = w'_{tide} + w'_{GW} + w'_{other} \tag{22}$$

The w'_{other} stands for the vertical wind perturbations due to sources other than atmospheric tide and gravity wave modulations. For instance, the chemical and dynamical transport velocities generated by wave dissipation and temperature variance (Gardner et al., 2014; Gardner & Liu, 2010), which is much smaller than the first two terms in equation (22) in the *E* and lower *F* region. In addition, w'_{other} may also include the perturbation caused by ion friction (Rishbeth & Garriott, 1969), which is outside the scope of this paper. We can estimate w'_{tide} and w'_{GW} to see which component can lead to large vertical wind perturbations. Based on Yuan et al. (2014), the measured semidiurnal and diurnal tidal vertical wind modulations (in all 12 months) are very small and no more than ~20 cm/s in most of the mesopause region (80–105 km), and CTMT is found to underestimate the tidal amplitude, as we mentioned in section 2.2. On the other hand, the downward phase progression of the number density of TSL observed (see the magenta line in Figure 1) matches well with the phase of atmospheric density modulation generated by the semidiurnal tide, suggesting that the large vertical wind perturbation is closely associated with the semidiurnal tide. Note that the observations of TSLs at ALO during equinox are fairly consistent on a yearly basis. Such consistent seasonal and local time variations resonate with those of tidal waves, suggesting a connection between TSLs and tidal waves in the *E* and lower *F* region. To test this hypothesis, we construct a neutral atmosphere with a large vertical wind perturbation based on CTMT outputs. Following the method in MacDougall et al. (2000) and Chu and Yu (2017), we assume that the amplitude of the vertical wind perturbation at $z_0 = 150$ km is 10 m/s. For those lower than 170 km, the vertical wind perturbation is $w(z) = w(z_0)\sqrt{\rho(z_0)/\rho(z)}$, where $\rho(z)$ is the atmospheric density at altitudes z apart from 150 km. Above 170 km, we assume that the vertical wind amplitude is constant ($w(z > 170\ km) = w(z > 170\ km)$). The largest amplitude of vertical wind perturbation becomes 16 m/s at 170 km. These efforts result in a new vertical wind perturbation that has a 12-hr period and follows the phase of the vertical wind modulation caused by CTMT semidiurnal tide. The maximum amplitude is 16 m/s at 170 km.

After defining the new vertical wind perturbation, we calculate the corresponding horizontal wind perturbations. First, we utilize both tide and gravity wave polarization relationships to derive horizontal wind perturbations and check whether the results are realistic. As for gravity waves, most of them occur irregularly. Based on Vadas and Fritts (2005) and Vadas (2007), only those waves with short periods (less than or equal to 5 hr) can propagate into high altitudes (>120 km). We utilize the polarization relationship in Vadas and

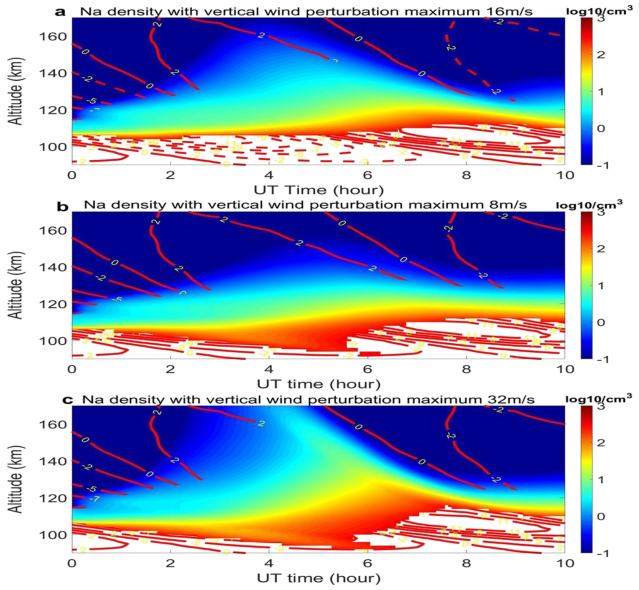

Figure 8. Time and altitude distribution of Na density over ALO with modified CTMT+24-hr mean of WACCMX-DART (color contours) and the density modulation due to semidiurnal tide over ALO (line contours) from CTMT. The maximum vertical wind perturbations are (a) 16 m/s, (b) 8 m/s, and (c) 32 m/s, respectively. Note that we multiply the original density modulation by 100. The Na number density is in log10 scale, while the density modulation contour is linear scale. The dashed line is the negative density modulation. The white area is the part where log10 of Na density larger than 2.5.

Fritts (2005) that already includes the dissipation mechanisms to calculate the corresponding horizontal wind perturbations with the above-mentioned vertical wind perturbations (16 m/s at 170 km). The results (>1,000 m/s) are far beyond the normal range of the thermospheric wind during geomagnetically quiet periods (absolute value <250 m/s) that have been reported by previous studies (Chartier et al., 2015; Emmert et al., 2002; Fisher et al., 2015; Häusler et al., 2007). Thus, the possibility of such large vertical wind perturbation solely due to gravity waves can be eliminated. For the tidal polarization relationship, until now there is only one study that deals with the nondissipating situation provided by She et al. (2016). We calculate the corresponding temperature perturbation for a 12-hr tidal wave, and the result for the 16-m/s vertical wind perturbation at 170 km is around 290 K, and the resulting horizontal wind perturbations are >4,000 m/s, both of which are too large to be realistic. Therefore, the tidal wave itself is impossible to generate that large vertical wind perturbation required to form TSL directly. However, the observed TSLs have very similar phase structure with the atmospheric density modulation generated by the semidiurnal tide. This fact suggests the existence of some unknown local perturbations with large-amplitude vertical wind perturbations associated with the semidiurnal tide in the E and lower F region at ALO. As is suggested by Liu (2017), large wind and shear can be generated mainly by mesoscale motions modulated by large-scale tidal waves near and above the mesopause region and these large winds and shear at a single location may display similar temporal variations attributable to tidal waves. Overall, the existing atmospheric wave polarization relationships cannot derive realistic horizontal wind perturbations based on 16-m/s vertical wind perturbation. To have a realistic estimation on horizontal wind perturbations, we need to check the horizontal wind data at ALO.

Figure 1 in Liu et al. (2016) depicts the observed TSL on 17 April 2015, extending up to 150 km. The lidar measured horizontal winds during the event, presented in Figure 4 in Liu et al. (2016), exhibits meridional winds with a peak value of 120 m/s around 130–140 km. It also shows a peak around 9:00–10:00 UT and a valley around 4:00 UT, which may suggest a perturbation with period 11 to 12 hr. Unfortunately, lidar signal to noise ratio in the zenith channel is too low to measure vertical wind above 105 km on that night.

Here we apply equations (7)–(12) in Fritts and Alexander (2003), which are the linearized type of fluid equations in Cartesian coordinate, to derive the associated horizontal perturbation with the large vertical wind perturbation that we proposed earlier. Although this perturbation is assumed to be local (scale smaller than the global tide), its horizontal scale can be quite large (several hundred or even thousand kilometers) because of its long period (at least 6 hr, estimated from Figure 1). Therefore, the horizontal gradient of the associated horizontal perturbation can be very small and the terms with perturbation derivatives in x and y directions in equations (7)–(12) in Fritts and Alexander (2003) can be ignored. In addition, the mean vertical wind is assumed to be zero. Finally, equations (7) and (8) in Fritts and Alexander (2003) can be rewritten as.

$$\frac{\partial U'}{\partial t} + W' \frac{\partial U_0}{\partial z} - fV' = 0, \tag{23}$$

$$\frac{\partial V'}{\partial t} + W' \frac{\partial V_0}{\partial z} - fU' = 0, \tag{24}$$

where U_0 and V_0 are the mean fields of zonal and meridional wind. W' is the constructed vertical wind perturbation with a peak amplitude of 16 m/s at 170 km and the phase following the semidiurnal tide phase. The mean fields and their shears can be adopted from WACCMX-DART, and the Coriolis frequency f =

$2\Omega\sin\varphi(\Omega = 7.29 \times 10^{-5} rad/s$ and $\varphi = 30°)$ is calculated at ALO. We can then derive the zonal and meridional wind perturbations (U' and V'). The amplitudes of resulting meridional and zonal wind perturbations are less than 80 m/s below 170 km. When the meridional wind perturbations are added to the mean field, the resulting meridional wind is 100–120 m/s at around 130–140 km, which is similar to observed meridional wind from Liu et al. (2016). By checking the lidar data, we utilize the observed wind from 90 to 104 km (vertical wind measurements only reach to 104 km) together with calculated horizontal winds (above 106 km). Now with all parameters determined, we run the extended 2-D model (the modeled perturbations and the diurnal mean from WACCMX-DART) from 0:00 UT to 10:00 UT (same as observation time range) and the result is depicted in Figure 8a. The resulting structure of the number density of Na between 120 and 170 km is similar to the observed TSLs: it has the same descending character and also matches well with the atmospheric density modulation generated by the semidiurnal tide in April at ALO from CTMT (contour line in Figure 8a). The positive semidiurnal tide density modulations (solid red line in Figure 8a) are slightly ahead of the Na number density maximum, in agreement with the results of Figure 1. However, the Na number density ($<2/cm^3$) in the simulation is lower than the $3–5/cm^3$ in the observed TSL. Unlike the simulated slow increase of number density during the night, the observed density appears to increase to $3–5/cm^3$ rather quickly. We have also run two additional cases (Figures 8b and 8c) with maximum vertical wind perturbations of 8 and 32 m/s and find that the Na layer density increases with the increase of the amplitude of vertical wind perturbation. However, the Na number density still decreases with altitude much faster than the observed TSL. This suggests that the actual vertical wind perturbation may be even larger than 32 m/s at these altitudes, or there may be some unknown mechanisms that can prevent the layer density diffusing with altitude. It should be noted that the amplitude of vertical wind perturbation cannot increase infinitely because the corresponding horizontal wind perturbations also increase and their combination with the mean field cannot exceed the normal range of thermospheric winds (<250 m/s). The Na^+ density variation during the same time (not shown here) is still similar to what is shown in Figure 2c because the horizontal wind amplitude does not change too much compared with the simulation using the neutral parameters from WACCMX-DART, and we use the same electric field.

The eddy diffusion term is also important for the Na layer in the MLT region (Cai et al., 2017; Marsh et al., 2013; Plane, 2004), and we have tested its effect on the formation of TSL at ALO. The eddy coefficient we adopt from Marsh et al. (2013) is a global mean and may not perfectly reflect the conditions of a mountain station, where large-amplitude small-scale gravity waves break and turbulence is known to occur. Thus, the local eddy diffusion profile may differ considerably from the global mean. To address this, we also performed simulations with a maximum vertical wind perturbation of 16 m/s but increased the eddy coefficient by 50 times. The TSL with 50 times eddy diffusion coefficient looks similar to the one with our default eddy coefficient (not shown here) above 120 km but differences in absolute sodium number densities do occur below this altitude. Therefore, the eddy diffusion does not appear to play a significant role in the formation of TSL, either.

4. Summary and Conclusions

By running a hybrid Na numerical model in the thermosphere, we are able to simulate the variations of Na and Na^+ in the equatorial E and F region during April above subtropical regions. With this extended 2-D model that includes neutral atmosphere (neutral winds and temperature), and electrodynamics conditions (electric field), we explore the underlying mechanism of the TSL observed at ALO in Chile during the spring equinox. The results of our work can be summarized as follows:

1. As the major reservoir of atomic Na in the E and lower F region, the distribution of Na^+ at ALO below 200 km is mainly controlled by vertical ion velocity. For the geomagnetic subtropical region (ALO), the vertical components of $\vec{E}\times\vec{B}$ drift and Coulomb-induced drift play significant roles in the variations of Na^+ structure during the night below 200 km. During daytime, the vertical ion velocity due to electric fields perpendicular to $\vec{B}$ together with vertical ion velocity due to the neutral wind prevents the formation of Na^+ layer above 130 km.
2. The TSL observed at ALO in April is closely associated with the semidiurnal tide, as it also shows downward phase progression that mainly follows the phase of tidal density modulation (within the range of day-to-day tidal phase variability). It is worth mentioning that the atmospheric density modulation

generated by semidiurnal tide peaks in April when most of the TSLs were observed. However, the vertical wind modulation generated by semidiurnal tide alone is too weak to resist the molecular diffusion to form the TSL, and the necessary large vertical wind perturbation could be related to some mesoscale dynamics, which would not be included in the global-scale models used in the present study. In other words, the appearance of TSL could indicate long-lasting large vertical wind perturbations (>10 m/s) in the *E* and lower *F* region. The models we utilize in this study may also need further improvements in order to reflect the large vertical wind perturbations realistically.

3. The fountain effect has little influence on the variations of Na at ALO, especially at night.
4. Horizontal neutral transport is able to enhance the number density of Na in the daytime below 120 km but does not facilitate the formation of the structure similar to TSL.
5. The most likely generation mechanism of TSL at ALO in the spring equinox is the large vertical neutral transport (equation (20)) caused by local mesoscale large vertical wind perturbations (such as 16 m/s at 170 km). This large vertical wind perturbation is closely associated with, but not directly generated by the semidiurnal tide. A large vertical wind perturbation is needed to resist the fast increase of molecular diffusion and other factors (such as gravity) in the thermosphere to transport neutral species upward.

Our numerical simulation has investigated the contributions of the horizontal transport, fountain effect, and recombination effect to the generation of the TSLs observed in April at ALO comprehensively. Based on these simulations, we propose that the large vertical wind perturbation induced vertical neutral transport (equation (20)) is critical for the formation of these TSLs. However, the source of such perturbation is still unclear. We can only construct the corresponding horizontal and vertical changes based on current simplified models and the sparse observations. Therefore, more observations and model studies of the temperature and neutral winds, especially between 120 and 200 km, are needed. Further improvement of this numerical framework is also necessary. For example, a global model that covers all components of transport would be required because the current zonal transport is simplified. In addition, it is necessary to derive the vertical wind by solving the full equation of thermospheric wind that includes all the factors such as ion friction and viscosity (Rishbeth & Garriott, 1969). A recent study revealed that the vertical wind perturbation in the lower thermosphere at low and middle latitudes could also be affected by geomagnetic activities (Li et al., 2018). Thus, future work will also include the contributions from geomagnetic activities. It is also possible that current Na ion-molecular chemistry theory in the literature is missing some critical chemical reactions in the thermosphere, leading to less chemical production of Na.

Acknowledgments

We highly appreciate the help of Oberheide at Clemson University with the CTMT models. We also want to thank Wuhu Feng at University of Leeds, UK, for providing the source function and eddy diffusion from WACCM-Na results used in this investigation. The discussions with H.-L. Liu, Sharon Vadas, Jeffery Forbes, and Xuewu Cheng also benefit greatly to this investigation. The discussion with Larry Gardner helps our numerical simulation. The ALO Na lidar data associated with this study can be found at this link: http://lidar.erau.edu/data/nalidar/index.php. The WACCMX-DART data and electric field data used in this study can be found at this link: https://works.bepress.com/xuguang_cai/. The CTMT data are available from http://globaldynamics.sites.clemson.edu/articles/ctmt.html. This study was performed as part of a collaborative research program supported under the Consortium of Resonance and Rayleigh Lidars (CRRL) National Science Foundation (NSF) grant 1135882, with additional support from NSF grants AGS1734333 and N000141712149 of the Naval Research Laboratory. The ALO lidar operation was supported by NSF grants AGS-1136208 and AGS-1136278. The National Center for Atmospheric Research is sponsored by the U.S. National Science Foundation. Vincent Eccles participation is funded through the Office of Naval Research grant N00014-17-1-2156.

References

Badnell, N. R. (2006). Radiative Recombination Data for Modeling Dynamic finite-density plasmas. *The Astrophysical Journal - Supplement Series*, *167*, 334–342. https://doi.org/10.1086/508465

Banks, P. M., & Kockarts, G. (1973). *Aeronomy, Part B*. New York: Academic Press.

Bilitza, D., Altadill, D., Zhang, Y., Mertens, C., Truhlik, V., Richards, P., et al. (2014). The international reference ionosphere 2012—A model of international collaboration. *Journal of Space Weather and Space Climate*, *4*, A07. https://doi.org/10.1051/swsc/2014004

Boris, J. P., & Book, D. L. (1973). Flux-corrected transport: I. SHASTA, a fluid transport algorithm that works. *Journal of Computational Physics*, *11*, 38–69. https://doi.org/10.1016/0021-9991(73)90147-2

Cai, X., Yuan, T., & Eccles, J. V. (2017). A numerical investigation on tidal and gravity wave contributions to the summer time Na variations in the midlatitude E region. *Journal of Geophysical Research: Space Physics*, *122*, 10–577. https://doi.org/10.1002/2016JA023764

Cai, X., Yuan, T., Eccles, J. V., & Raizada, S. (2019). Investigation on the distinct nocturnal secondary sodium layer behavior above 95 km in winter and summer over Logan, UT (41.7°N, 112°W) and Arecibo Observatory, PR (18.3°N, 67°W). *Journal of Geophysical Research: Space Physics*. https://doi.org/10.1029/2019ja026746

Carter, L. N., & Forbes, J. M. (1999). Global transport and localized layering of metallic ions in the upper atmosphere. *Annals of Geophysics*, *17*(2), 190–209. https://doi.org/10.1007/s00585-999-0190-6

Chartier, A. T., Makela, J. J., Liu, H., Bust, G. S., & Noto, J. (2015). Modeled and observed equatorial thermospheric winds and temperatures. *Journal of Geophysical Research: Space Physics*, *120*, 5832–5844. https://doi.org/10.1002/2014JA020921

Chu, X., & Yu, Z. (2017). Formation mechanisms of neutral Fe layers in the thermosphere at Antarctica studied with a thermosphere-ionosphere Fe/Fe^+ (TIFe) model. *Journal of Geophysical Research: Space Physics*, *122*, 6812–6848. https://doi.org/10.1002/2016JA023773

Chu, X., Yu, Z., Gardner, C. S., Chen, C., & Fong, W. (2011). Lidar observations of neutral Fe layers and fast gravity waves in the thermosphere (110–155 km) at McMurdo (77.8°S, 166.7°E), Antarctica. *Geophysical Research Letters*, *38*, L23807. https://doi.org/10.1029/2011GL050016

Clemesha, B. R. (1995). Sporadic neutral metal layers in the mesosphere and lower thermosphere. *Journal of Atmospheric and Terrestrial Physics*, *57*(7), 725–736. https://doi.org/10.1016/0021-9169(94)00049-t

Cox, R. M., & Plane, J. M. C. (1998). An ion-molecule mechanism for the formation of neutral sporadic Na layers. *Journal of Geophysical Research*, *103*(D6), 6349–6359. https://doi.org/10.1029/97JD03376

Daire, S. E., Plane, J. M. C., Gamblin, S. D., Soldn, P., Lee, E. P. F., & Wright, T. G. (2002). A theoretical study of the ligand-exchange reactions of Na^+X complexes (X = O, O_2, N_2, CO_2 and H_2O): Implications for the upper atmosphere. *Journal of Atmospheric and Solar - Terrestrial Physics*, *64*, 863–870. https://doi.org/10.1016/S1364-6826(02)00130-X

Delgado, R., Friedman, J. S., Fentzke, J. T., Raizada, S., & Tepley, C. A. (2012). Sporadic metal atom and ion layers and their connection to chemistry and thermal structure in the mesopause region at Arecibo. *Journal of Atmospheric and Solar - Terrestrial Physics*, *74*, 11–23. https://doi.org/10.1016/j.jastp.2011.09.004

Dou, X. K., Xue, X. H., Li, T., Chen, T. D., Chen, C., & Qiu, S. C. (2010). Possible relations between meteors, enhanced electron density layers, and sporadic sodium layers. *Journal of Geophysical Research*, *115*, A06311. https://doi.org/10.1029/2009JA014575

Eccles, J. V. (1998). Modeling investigation of the evening prereversal enhancement of the zonal electric field in the equatorial ionosphere. *Journal of Geophysical Research*, *103*, 26,709–26,720. https://doi.org/10.1029/98ja02656

Emmert, J. T., Fejer, B. G., Shepherd, G. G., & Solheim, B. H. (2002). Altitude dependence of middle and low-latitude daytime thermospheric disturbance winds measured by WINDII. *Journal of Geophysical Research*, *107*(A12), 1483. https://doi.org/10.1029/2002JA009646

Fisher, D. J., Makela, J. J., Meriwether, J. W., Buriti, R. A., Benkhaldoun, Z., Kaab, M., & Lagheryeb, A. (2015). Climatologies of nighttime thermospheric winds and temperatures from Fabry-Perot interferometer measurements: From solar minimum to solar maximum. *Journal of Geophysical Research: Space Physics*, *120*, 6679–6693. https://doi.org/10.1002/2015JA021170

Forbes, J. M., Zhang, X., & Bruinsma, S. L. (2014). New perspectives on thermospheric tides: 2. Penetration to the upper thermosphere. *Earth, Planets and Space*, *66*(1), 1–11. https://doi.org/10.1186/1880-5981-66-122

Forbes, J. M., Zhang, X., Palo, S., Russell, J., Mertens, C. J., & Mlynczak, M. (2008). Tidal variability in the ionospheric dynamo region. *Journal of Geophysical Research*, *113*, A02310. https://doi.org/10.1029/2007JA012737

Friedman, J. S., Chu, X., Brum, C. G. M., & Lu, X. (2013). Observation of a thermospheric descending layer of neutral K over Arecibo. *Journal of Atmospheric and Solar - Terrestrial Physics*, *104*, 253–259. https://doi.org/10.1016/j.jastp.2013.03.002

Friedman, J. S., Gon'zalez, S. A., Tepley, C. A., Zhou, Q., Sulzer, M. P., Collins, S. C., & Grime, B. W. (2000). Simultaneous atomic and ion layer enhancements observed in the mesopause region over Arecibo during the Coqui II sounding rocket campaign. *Geophysical Research Letters*, *27*, 449–452. https://doi.org/10.1029/1999gl900605

Gao, Q., Chu, X., Xue, X., Dou, X., Chen, T., & Chen, J. (2015). Lidar observations of thermospheric Na layers up to 170 km with a descending tidal phase at Lijiang (26.7°N, 100.0°E), China. *Journal of Geophysical Research: Space Physics*, *120*, 9213–9220. https://doi.org/10.1002/2015JA02180

Gardner, C. S. (2004). Performance capabilities of middle-atmosphere temperature lidars: Comparison of Na, K, Ca, Ca+, and Rayleigh systems. *Applied Optics*, *43*(25), 4941–4956. https://doi.org/10.1364/ao.43.004941

Gardner, C. S., & Liu, A. Z. (2010). Wave-induced transport of atmospheric constituents and its effect on the mesospheric Na layer. *Journal of Geophysical Research*, *115*, D20302. https://doi.org/10.1029/2010JD014140

Gardner, C. S., Liu, A. Z., Marsh, D. R., Feng, W., & Plane, J. M. C. (2014). Inferring the global cosmic dust influx to the Earth's atmosphere from lidar observations of the vertical flux of mesospheric Na, J. Geophys. Res. *Space Physics*, *119*, 7870–7879. https://doi.org/10.1002/2014JA020383

Gardner, C. S., Plane, J. M. C., Pan, W., Vondrak, T., Murray, B. J., & Chu, X. (2005). Seasonal variations of the Na and Fe layers at the south pole and their implications for the chemistry and general circulation of the polar mesosphere. *Journal of Geophysical Research*, *110*, D10302. https://doi.org/10310.11029/12004JD005670

Gumbel, J., Fan, Z. Y., Waldemarsson, T., Stegman, J., Witt, G., Llewellyn, E. J., et al. (2007). Retrieval of global mesospheric sodium densities from the Odin satellite. *Geophysical Research Letters*, *34*, L04813. https://doi.org/10.1029/2006GL028687

Haerendel, G., Eccles, J. V., & Çakir, S. (1992). Theory for modeling the equatorial evening ionosphere and the origin of the shear in the horizontal plasma flow. *Journal of Geophysical Research*, *97*, 1209. https://doi.org/10.1029/91ja02226

Häusler, K., Hagan, M. E., Forbes, J. M., Zhang, X., Doornbos, E., Bruinsma, S., & Lu, G. (2015). Intra-annual variability of tides in the thermosphere from model simulations and in situ satellite observations. *Journal of Geophysical Research: Space Physics*, *120*, 751–765. https://doi.org/10.1002/2014JA020579

Häusler, K., Lühr, H., Rentz, S., & Köhler, W. (2007). A statistical analysis of longitudinal dependences of upper thermospheric zonal winds at dip equator latitudes derived from CHAMP. *Journal of Atmospheric and Solar - Terrestrial Physics*, *69*, 1419–1430. https://doi.org/10.1016/j.jastp.2007.04.004

Heinrich, D., Nesse, H., Blum, U., Acott, P., Williams, B., & Hoppe, U.-P. (2008). Summer sudden Na number density enhancements measured with the ALOMAR weber Na Lidar. *Annals of Geophysics*, *26*, 1057–1069.

Kelley, M. C. (2009). *The Earth's Ionosphere: Plasma Physics & Electrodynamics*, (Vol. 96). San Diego, Calif: Academic Press.

Larsen, M. F., & Meriwether, J. W. (2012). Vertical winds in the thermosphere. *Journal of Geophysical Research*, *117*, A09319. https://doi.org/10.1029/2012JA017843

Li, J., Wang, W., Lu, J., Yuan, T., Yue, J., Liu, X., et al. (2018). On the responses of mesosphere and lower thermosphere temperatures to geomagnetic storms at low and middle latitudes. *Geophysical Research Letters*, *45*. https://doi.org/10.1029/2018GL078968

Liu, A. Z., Guo, Y., Vargas, F., & Swenson, G. R. (2016). First measurement of horizontal wind and temperature in the lower thermosphere (105–140 km) with a Na Lidar at Andes Lidar observatory. *Geophysical Research Letters*, *43*, 2374–2380. https://doi.org/10.1002/2016GL068461

Liu, H.-L. (2017). Large wind shears and their implications for diffusion in regions with enhanced static stability: The mesopause and the tropopause. *Journal of Geophysical Research: Atmospheres*, *122*, 9579–9590. https://doi.org/10.1002/2017JD026748

Lübken, F.-J., Höffner, J., Viehl, T. P., Kaifler, B., & Morris, R. J. (2011). First measurements of thermal tides in the summer mesopause region at Antarctic latitudes. *Geophysical Research Letters*, *38*, L24806. https://doi.org/10.1029/2011GL050045

MacDougall, J. W., Plane, J. M. C., & Jayachandran, P. T. (2000). Polar cap sporadic-E: Part 2. Modeling. *Journal of Atmospheric and Solar - Terrestrial Physics*, *62*, 1169–1176.

Marsh, D. R., Janches, D., Feng, W., & Plane, J. M. C. (2013). A global model of meteoric sodium. *Journal of Geophysical Research: Atmospheres*, *118*, 11,442–11,452. https://doi.org/10.1002/jgrd.50870

Oberheide, J., Forbes, J. M., Zhang, X., & Bruinsma, S. L. (2011). Climatology of upward propagating diurnal and semidiurnal tides in the thermosphere. *Journal of Geophysical Research*, *116*, A11306. https://doi.org/10.1029/2011JA016784

Pedatella, N. M., Liu, H.-L., Marsh, D. R., Raeder, K., Anderson, J. L., Chau, J. L., et al. (2018). Analysis and hindcast experiments of the 2009 sudden stratospheric warming in WACCMX+DART. *Journal of Geophysical Research: Space Physics*, *123*, 3131–3153. https://doi.org/10.1002/2017JA025107

Pedatella, N. M., Raeder, K., Anderson, J. L., & Liu, H.-L. (2014). Ensemble data assimilation in the whole atmosphere community climate model. *Journal of Geophysical Research: Atmospheres*, *119*, 9793–9809. https://doi.org/10.1002/2014JD021776

Plane, J. M. C. (2004). A time-resolved model of the mesospheric Na layer: Constraints on the meteor input function. *Atmospheric Chemistry and Physics*, *4*, 627–638. https://doi.org/10.5194/acp-4-627-2004

Plane, J. M. C., Feng, W., & Dawkins, E. C. M. (2015). The mesosphere and metals: Chemistry and changes. *Chemical Reviews*, *115*(10), 4497–4541. https://doi.org/10.1021/cr500501m

Rishbeth, H., & Garriott, O. K. (1969). *Introduction to Ionospheric Physics*, 331 pp., New York: Elsevier.

Schunk, R. W., & Nagy, A. F. (2009). *Ionospheres: Physics, Plasma Physics, and Chemistry*. Cambridge, UK: Cambridge University Express.

She, C. Y., Chen, S., Hu, Z., Sherman, J., Vance, J. D., Vasoli, V., et al. (2000). Eight-year climatology of nocturnal temperature and sodium density in the mesopause region (80 to 105 km) over Fort Collins, CO (41°N, 105°W). *Geophysical Research Letters*, *27*, 3289–3292. https://doi.org/10.1029/2000GL003825

She, C.-Y., Krueger, D. A., Yuan, T., & Oberheide, J. (2016). On the polarization relations of diurnal and semidiurnal tide in the mesopause region. *Journal of Atmospheric and Solar - Terrestrial Physics*, *142*, 60–71. https://doi.org/10.1016/j.jastp.2016.02.024

States, R. J., & Gardner, C. S. (1999). Structure of the mesospheric Na layer at 40°N latitude: Seasonal and diurnal variations. *Journal of Geophysical Research*, *104*, 11,783–11,798. https://doi.org/10.1029/1999jd900002

Tsuda, T. T., Chu, X., Nakamura, T., Ejiri, M. K., Kawahara, T. D., Yukimatu, A. S., & Hosokawa, K. (2015). A thermospheric Na layer event observed up to 140 km over Syowa Station (69.0°S, 39.6°E) in Antarctica. *Geophysical Research Letters*, *42*, 3647–3653. https://doi.org/10.1002/2015GL064101

Vadas, S. L. (2007). Horizontal and vertical propagation and dissipation of gravity waves in the thermosphere from lower atmospheric and thermospheric sources. *Journal of Geophysical Research*, *112*, A06305. https://doi.org/10.1029/2006JA011845

Vadas, S. L., & Fritts, D. C. (2005). Thermospheric responses to gravity waves: Influences of increasing viscosity and thermal diffusivity. *Journal of Geophysical Research*, *110*, D15103. https://doi.org/10.1029/2004JD005574

Vondrak, T., Plane, J. M. C., Broadley, S., & Janches, D. (2008). A chemical model of meteoric ablation. *Atmospheric Chemistry and Physics*, *8*(23), 7015–7031. https://doi.org/10.5194/acp-8-7015-2008

Wang, J., Yang, Y., Cheng, X., Yang, G., Song, S., & Gong, S. (2012). Double sodium layers observation over Beijing, China. *Geophysical Research Letters*, *39*, L15801. https://doi.org/10.1029/2012GL052134

Wang, W., Burns, A. G., Wiltberger, M., Solomon, S. C., & Killeen, T. L. (2008). Altitude variations of the horizontal thermospheric winds during geomagnetic storms. *Journal of Geophysical Research*, *113*, A02301. https://doi.org/10.1029/2007JA012374

Xue, X. H., Dou, X. K., Lei, J., Chen, J. S., Ding, Z. H., Li, T., et al. (2013). Lower thermospheric-enhanced sodium layers observed at low latitude and possible formation: Case studied. *Journal of Geophysical Research: Space Physics*, *118*, 2409–2418. https://doi.org/10.1002/jgra.50200

Yi, F., Yu, C., Zhang, S., Yue, X., He, Y., Huang, C., et al. (2009). Seasonal variations of the nocturnal mesospheric Na and Fe layers at 30°N. *Journal of Geophysical Research*, *114*, D01301. https://doi.org/10.1029/2008JD010344

Yi, F., Zhang, S., Yu, C., He, Y., Yue, X., Huang, C., & Zhou, J. (2007). Simultaneous observations of sporadic Fe and Na layers by two closely collocated resonance fluorescence lidars at Wuhan (30.5°N, 114.4°E), China. *Journal of Geophysical Research*, *112*, D04303. https://doi.org/10.1029/2006JD007413

Yuan, T., Fish, C., Sojka, J., Rice, D., Taylor, M. J., & Mitchell, N. J. (2013). Coordinated investigation of summer time mid-latitude descending E layer (Es) perturbations using Na lidar, ionosonde, and meteor wind radar observations over Logan, Utah (41.7°N, 111.8°W). *Journal of Geophysical Research: Atmospheres*, *118*, 1734–1746. https://doi.org/10.1029/2012JD017845

Yuan, T., She, C. Y., Forbes, J., Zhang, X., Krueger, D., & Reising, S. (2010). A collaborative study on temperature diurnal tide in the midlatitude mesopause region (41°N, 105°W) with Na lidar and TIMED/SABER observations. *Journal of Atmospheric and Solar - Terrestrial Physics*, *72*, 541–549. https://doi.org/10.1016/j.jastp.2010.06.012

Yuan, T., She, C.-Y., Kawahara, T. D., & Krueger, D. A. (2012). Seasonal variations of mid-latitude mesospheric Na layer and its tidal period perturbations based on full-diurnal-cycle Na lidar observations of 2002–2008. *Journal of Geophysical Research*, *117*, D11304. https://doi.org/10.1029/2011JD017031

Yuan, T., She, C. Y., Oberheide, J., & Krueger, D. A. (2014). Vertical tidal wind climatology from full-diurnal-cycle temperature and Na density lidar observations at Ft. Collins, CO (41°N, 105°W). *Journal of Geophysical Research: Atmospheres*, *119*, 4600–4615. https://doi.org/10.1002/2013JD020338

Yuan, T., Wang, J., Cai, X., Sojka, J., Rice, D., Oberheide, J., & Criddle, N. (2014). Investigation of the seasonal and local time variations of the high-altitude sporadic Na layer (Nas) formation and the associated midlatitude descending E layer (Es) in lower E region. *Journal of Geophysical Research: Space Physics*, *119*, 5985–5999. https://doi.org/10.1002/2014JA019942

Zalesak, S. T. (1979). Fully multidimensional flux-corrected transport algorithms for flfluids. *Journal of Computational Physics*, *31*, 335–362. https://doi.org/10.1016/0021-9991(79)90051-2